Inorganic Chemistry

Article

pubs.acs.org/IC

# Mixed Metallic Ba(Co,Fe)$X_{0.2}O_{3-\delta}$ (X = F, Cl) Hexagonal Perovskites: Drastic Effect of Fe-Incorporation on Structural and Electronic Features

Mihaela Iorgulescu,[†] Pascal Roussel,[†] Nathalie Tancret,[†] Nicolas Renault,[†] Florence Porcher,[‡] Gilles André,[‡] Houria Kabbour,[†] and Olivier Mentré[†,*]

[†]Université Lille Nord de France, UCCS, CNRS UMR 8181, ENSCL-USTL, Villeneuve d'Ascq, France

[‡]Laboratoire Léon-Brillouin (LLB), CEA-Saclay, bât. 563-91191 Gif-sur-Yvette Cedex, France

Supporting Information

**ABSTRACT:** Starting from the parent 10H−$Ba_5Co_5X_{1-x}O_{13-\delta}$ (trimeric strings of face-sharing $CoO_6$ octahedra with terminal $CoO_4$ tetrahedra, stacking sequence $(chhch')_2$) and 6H−$Ba_6Co_6X_{1-x}O_{16-\delta}$ (similar with tetrameric strings, stacking sequence chhhch') hexagonal perovskites forms (X = F, Cl; *c*, *h* = $[BaO_3]$ layers ; *h'* = $[BaOX_{1-y}]$ layers), we show here that the Fe incorporation leads to large domains of solid solutions for both X = F and Cl but exclusively stabilizes the 10H-form independently of the synthesis method. In this form, the lowest concentration of h-layers is stabilized by a sensitive metal reduction with increasing the Fe ratio. In a more general context of competition between several hexagonal perovskite polymorphs available for most of the transition metals, this redox change is most probably the key factor driving 1D (face-sharing chains) to 3D (corner-sharing) connectivities. Strikingly, ND data evidence the location of oxygen deficiencies in the tetrahedral (Co/Fe) coordination. This effect is exaggerated at high temperature, while $(Co/Fe)O_{4-\delta}$ coordinations are completed by the displacement of $X^-$ anions toward the (Co/Fe) sphere of coordination following a "*push-and-pull*" mechanism within *h'*−$[BaOX_{1-y}]$ layers. The Fe-incorporation is also accompanied by increasing conduction gaps with predominant 1D variable range hopping. The full series show antiferromagnetic behavior with increasing $T_N$ as [Fe] increases. For Fe-rich compounds $T_N$ is estimated about 600 K, as rarely observed for hexagonal perovskite compounds. Finally, magnetic structures of all iron-doped compounds show a site-to-site AFM ordering, different of the magnetic structure of Co-only parent compounds. Here, DFT calculations predict low-spin octahedral Co configurations, but high-spin Fe species in the same sites.

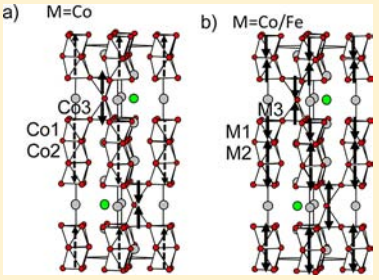


## 1. INTRODUCTION

The perovskite structure of ideal formula $ABO_3$ can be built from two extreme close-packing types of $AO_3$ layers with the B cations in the octahedral holes: (i) the cubic stacking (*abcabc*) sequence, with all $BO_6$ octahedra sharing corners within the *ccc* (=3C) framework, where *c* refers to the cubic layers, e.g., $BaTiO_3$,[1] and (ii) the hexagonal (*abab*) sequence with octahedral B cations sharing faces into infinite one-dimensional chains within the *hh* (=2H) hexagonal polytype, e.g., $BaCoO_3$.[2] Between these two extreme forms, a multitude of intermediate hexagonal structures with sizable proportions of *c* and *h* layers can be formed.[3] Deficient layers such as $[BaO_2]$, [BaO], [BaOCl], etc. can also be combined to $[BaO_3]$ layers into a great number of modified sequences derived from hexagonal perovskites. Recently, a series of modular halogeno-cobaltites has been evidenced in which the slicing between individual blocks is achieved by $[BaOX_{1-x}]$ (X = F, Cl)[4]) or $[Ba_2O_2X]$ (X = Br) halogeno-layers[5] that create terminal $CoO_4$ tetrahedra similarly to what is found in the 5H and 12H forms of deficient $BaCoO_{3-\delta}$ oxides.[6] Then the connectivity between the blocks at the tetrahedral level depends on the nature of the central anionic layer, i.e., disconnected on both sides of $[BaO_2]$ layers in deficient oxides, connected through dimeric $Co_2O_7$ bridges for $[BaOX_{1-x}]$ (X = F, Cl) layers, and strongly disconnected for $[Ba_2O_2X]$ (X = Br) double layers. Strikingly, in all the mentioned compounds, the elementary blocks display intrinsic ferromagnetism (FM) while the total magnetism depends on the interblock connectivity topical of a modular magnetic behavior: FM-oxides, AFM oxo-chlorides and oxo-fluorides,and spin-flipping oxo-bromides[7] (Figure 1). This behavior associated with the phases in competition open wide roads for predictable magnetic materials through pertinent intergrowths. However, at the moment, a full rationalization of the competing phenomena is far to be established because it is dominated by a number of casual exceptions. For instance, it is worth noting that in the series of Co-oxides and Co-oxo-halides, the elementary blocks systematically contain either trimeric (*n* = 3) or tetrameric (*n* = 4) linear strings of face-sharing octahedra while all other *n* values could be expected, taking into account the filiations of these compounds with the parent mono-dimensional 2H-$BaCoO_3$ compound (*n* = ∝). This observation, even if not well rationalized, appears specific of cobalt compounds since other string lengths are more stable

**Received:** February 22, 2012
**Published:** June 27, 2012

   dx.doi.org/10.1021/ic3004068 | *Inorg. Chem.* 2012, 51, 7598−7608

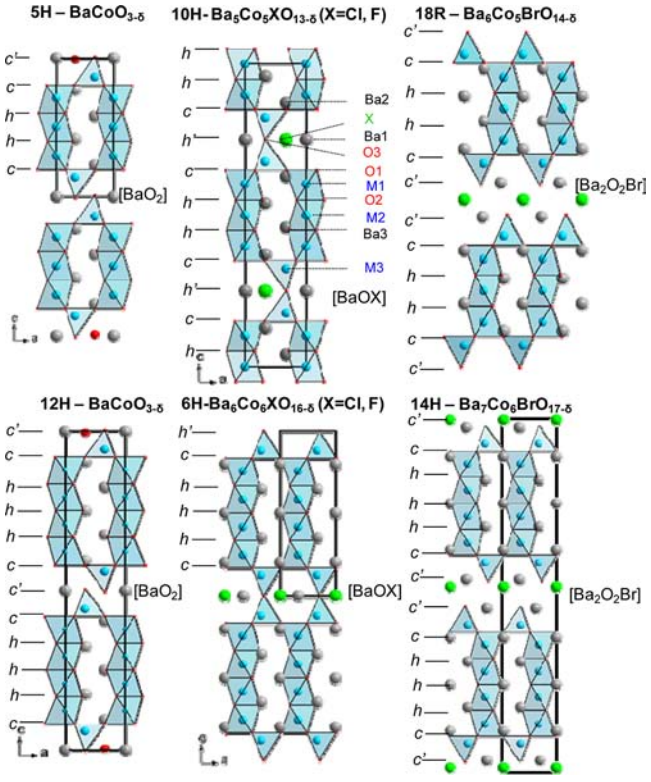


**Figure 1.** Related trimeric and tetrameric polytypes in the Ba−Co−X−O system with the stacking sequence. For the 10H-system the atom label scheme used in this work is given.

for similar systems with different transition metals ($n$ = 6 in $Ba_8Co_2Mn_6ClO_{22-\delta}$,[8] $n$ = 2 to 5 in $BaMnO_{3-\delta}$,[9] $n$ = 2 to 3 in $BaFeO_{3-\delta}$.[10] At least, if one considers one by one the Ba−M−O−X chemical systems, the concentration of $h$-face-sharing layers intuitively increases (i.e., the ratio $h/c$ increases) with the mean oxidation number of M, according to the tolerance factor commonly given by $t = (r_A + r_O)/[2(r_B + r_O)]^{1/2}$, factor which is deviated into the hexagonal range ($t > 1$) for the smallest oxidized M cations (i.e., with smallest $r_B$). This empirical law seems rather well respected for most of the metals (see $c/h$ sequence in the $BaMnO_{3-\delta}$ polytypes versus the oxygen vacancies)[9] but once more raises questions about a general model for the location of oxygen vacancies. It is noteworthy that in Ba−Co-oxides and Ba−Co-oxo-halides mainly of the oxygen vacancies agglomerate in deficient ordered layers such as $c'$-[$BaO_2$] or $h'$-[BaOX], singularly all the $BaMnO_{3-\delta}$ polytypes (15R, 8H, 10H, 6H, 4H) factually show, according to neutron diffraction data, a strong preference for oxygen deficiency in hexagonal $h$−[$BaO_{3-\delta}$] layers, contradictory to what is expected from the lower ratio of $h$-layers for more reduced compounds.[11] Then, new data involving mixed metallic systems should give informative insights for a rational globalization of extended chemical systems. In this paper, we report the synthesis and full structural, magnetic, and electrical characterization of the solid−solutions $Ba_5Co_{5-y}Fe_yX_{1-x}O_{13-\delta}$ ($y$ = 1 to 3 for X = F and $y$ = 1 to 4 for X = Cl). New results about their redox and thermal stability properties will give new arguments toward a global panorama about the expected polytypes and prediction of oxygen vacancies location. Also transport and magnetic properties have been investigated and show drastic effects as soon as a little amount of Fe is incorporated in the parent oxo-halides Co-structure.

## 2. EXPERIMENTAL PROCEDURES

The synthesis of $Ba_5Co_{5-y}Fe_yXO_{13-\delta}$ (X = F and Cl and $y$ = 1 to 5) was performed as follows: a stœchiometric mixture of $BaCO_3$ (Sigma-Aldrich, 99%), $Co_3O_4$ (Alfa Aesar, 99.7%), $Fe_2O_3$ (Prolabo, 99%), $BaF_2$ (Prolabo, 99%) (for X = F) or $BaCl_2$, $2H_2O$ (Prolabo, 99%) (for X=Cl) was heated in air at 900 °C (F case)/1000 °C (Cl case) for 24 h(F)/48 h(Cl) in an alumina crucible after preliminary grinding. The mixture was then cooled to room temperature in 6 h. Note that quenching in air leads to the same final products. For X = F, the compound $y$ = 4 was not obtained pure but in a mixture with a 15R form reported elsewhere.[12] The products were obtained as dark powders characterized by powder X-ray diffraction (XRD) using a D8 Bruker diffractometer, CuK$\alpha$ radiation. The mean oxidation states of Co/Fe were determined by iodometric titration. The error on each titration is estimated to ox. number ± 0.01 from both the experimental precision and the statistic deviation from four subsequent titrations on each batch. These results are listed in the Table 1. For $y$ = 0, 1, 2, 3 (X = F) and $y$ = 0, 4 (X = Cl), we benefited from neutron diffraction data at room temperature (high resolution 3T2 diffractometer, $\lambda$ = 1.225 Å, Laboratoire Léon Brillouin, Saclay, France). The same compounds were also investigated by low-temperature neutron diffraction using the LLB G4.1 diffractometer ($\lambda$ = 2.4226 Å). The profile refinement, nuclear structure refinement, and magnetic structure refinement were performed using the FullProf program.[13] The high temperature XRD data were also performed using an Anton Paar XRK900 chamber. The magnetic susceptibility was investigated using a Vibration Sample Magnetometer (VSM), under air or flowing nitrogen. The electrical properties were measured by the four points method, from RT to 7 K using a helium-free ARS cryostat. Thermogravimetric analysis (TGA) and differential thermal analysis (DTA) were carried out using a combined TG-DTA 92-1600 SETARAM analyzer. Successive heating/cooling cycles were performed using a rate of 5 °C/min.

Density functional theory (DFT)-based electronic structure calculations were performed using the Vienna ab initio simulation package (VASP).[14] The calculations were carried out within the generalized gradient approximation (GGA) for the electron exchange and correlation corrections using the Perdew−Wang[15] functional and the frozen core projected wave vector method.[16] The total energies calculations were performed on the substituted theoretical model $Ba_5Fe_2Co_3O_{13}F$ using a site-to-site antiferromagnetic configuration along the string direction. A plane wave energy cutoff of 400 eV, a total energy convergence threshold of $10^{-6}$, and 24 $k$ points in the irreducible Brillouin zone were used.

Numerous aspects of the prepared compounds have been investigated using the confrontation between several techniques. Generally, for each $Ba_5Co_{5-y}Fe_yX_{x-1}O_{13\sim\delta}$ compound, the $x$, $y$, $\delta$ data set was deduced from experimental results or approximated when particular analyzes (such as ND data) were not available. In general, the $x$ halide ratio was either refined from ND data leading to values very close to the expected $x$ = 1 value, either assumed to be 1. The $y$ Fe versus Co distribution is defined from the experimental stoichiometry and verified from ND data when available. The oxygen $\delta$ nonstoichiometry was calculated from redox titration performed just after synthesis and from ND data performed with variable time after synthesis. We note that for several compositions, long-time air exposure was voluntary applied to the samples. Here also, titration was applied and show sensitive redox changes. In general, the TGA of those exposed samples show a particular behavior during the primary heating but then come back to their initial "as-prepared" state from subsequent titration results. Our strategy with addition of the additional structural and properties characterizations are schematized in Figure 2. In the Supporting Information Table S1 are listed the individual experiments performed or not on all the investigated samples.

## 3. STRUCTURAL FEATURES

**3.a. Polytypes in Competition.** We have mentioned in the Introduction the duality between strings of $n$ = 3 versus $n$ = 4


dx.doi.org/10.1021/ic3004068 | Inorg. Chem. 2012, 51, 7598−7608

**Table 1. Preparation of $Ba_5(Co,Fe)_5X_{1-x}O_{13-\delta}$ Series with the Obtained Structural Type, Refined Cell Parameters, and Space Groups[a]**

| y (Fe) | X | synthesis | structural type | lattice parameters (Å) | Titration after synthesisO.D. O.C. |
|---|---|---|---|---|---|
| | Cl | | | | |
| 0 | 1 | air, 900 °C,48 h 1030 °C, 48 h, quench | 10H | a = 5.660(9), c = 24.300(5) | +3.24(1) 12.61 |
| 1 | 1 | air, 1000 °C, 24 h | 10H | a = 5.697(9), c= 24.357(5) | +3.19(1) 12.47 |
| 2 | 1 | air, 1000 °C, 24 h | 10H | a = 5.718(7), c = 24.428(4) | +3.19(1) 12.46 |
| 3 | 0.6 | air, 1000 °C, 24 h | 10H | a = 5.745(2), c = 24.454(4) | +3.04(1) 12.10 |
| | 0.7 | air, 1000 °C, 24 h | 10H | a = 5.739(2), c = 24.449(4) | +3.13(1) 12.33 |
| | 1 | air, 1000 °C, 24 h | 10H | a = 5.741(5), c = 24.528(3) | +3.18(1) 12.43 |
| 4 | 1 | air, 1000 °C, 24 h, gold tube | 10H | a = 5.759(6), c = 24.574(3) | +3.17(1) 12.43 |
| | 1 | air, 1000 °C, 24 h | 10H+ $Ba_3Fe_2Cl_2O_5$ ($I2_13$) | a = 5.7623(3), c = 24.592(2) a = 9.971(3) | |
| 5 | 0.5 | gold tube, 900 °C, 48 h,quench | 10H | a = 5.781(1), c = 24.614(1) | +3.13(1) 12.30 |
| | F | | | | |
| 0 | 1 | gold tube, 1030 °C, 72 h, quench | 10H ($P6_3/mmc$) | a = 5.681(8), c = 23.700(5) | +3.20(1) 12.50 |
| 1 | 1 | air, 900 °C, 24 h | 10H | a = 5.690(9), c = 23.921(5) | +3.16(1) 12.40 |
| 2 | 1 | air, 900 °C, 24 h | 10H | a = 5.711(1), c = 23.981(6) | +3.16(1) 12.38 |
| 3 | 0.6 | gold tube, 950 °C, 48 h, quench | 10H | a = 5.744(5), c = 24.120(2) | +3.29(1) 12.74 |
| | 1 | air, 900 °C, 24 h | 10H | a = 5.730(1), c = 24.087(4) | +3.15(1) 12.37 |
| 4 | 1 | air, 900 °C, 24 h | 10H + 15R($R\bar{3}m$) | a = 5.731(1), c = 24.087(4) + a = 5.753(8), c = 36.234(6) | |

[a]The initial iodometric-titrated oxidation degrees (O.D.) and oxygen content (O.C.) are listed as well as after the TG analyses.

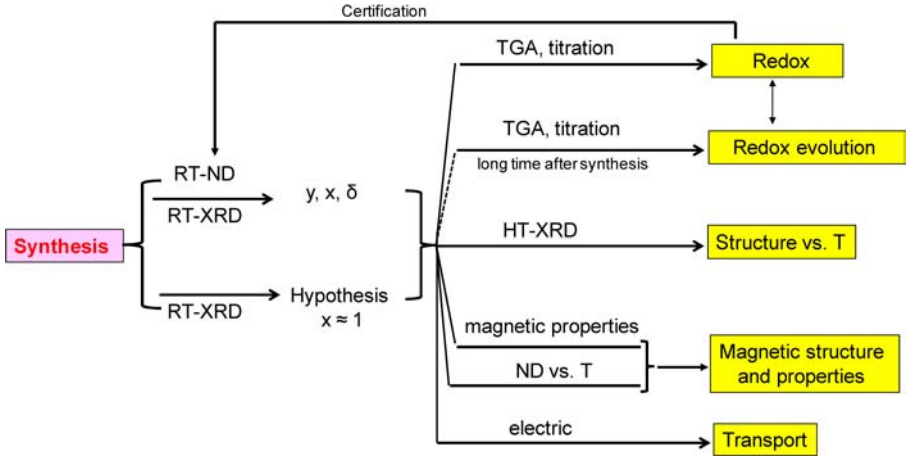


**Figure 2.** Summarized schema showing the different analyses performed on the $Ba_5Co_{5-y}Fe_yX_{1-x}O_{13-\delta}$ compounds and obtained informations.

face-sharing octahedra in Ba−Co−O−X systems. This aspect is reinforced because mixed M/M′ oxides also show similar string lengths, e.g., 12H−$BaMn_{0.4}Co_{0.6}O_{2.83}$ ($n$ = 4, full sequence $(chhhcc')_2$),[17] 5H−$BaMn_{0.2}Co_{0.8}O_{2.80}$ ($n$ = 3, full sequence $(chhcc')$),[18] the 10H−$BaMn_{0.4}Fe_{0.6}O_{2.73}$ (($n$ = 3, full sequence $(chhch')_2$),[19] and the Mn-rich 6H−$BaMn_{1-x}Fe_xO_{3-\delta}$ ($n$ = 4, full sequence $(chhhch)$),[20] but this seems to indicate an unpredictable tendency for the crystal form. Clearly, in the context of our work, the introduction of $h'$-[BaOX]-layers orientates the possibilities toward only the 10H (($n$ = 3, full sequence $(chhch')_2$) and 6H polytypes ($n$ = 4, full sequence $(chhhch')$) polytypes.

*Parent Co-Oxohalides.* The 6H−$Ba_6Co_6XO_{13-\delta}$ (X = F, Cl) are prepared in air atmosphere by slow cooling from 900 °C to room temperature. Both halides lead to a strong reduction on heating and transform into the 10H-form above 1000 °C; a quenching at this temperature stabilizes the single-phased 10H (trimeric) form (Figure 3). It comforts the more reduced character of the trimeric form, in good agreement with our


dx.doi.org/10.1021/ic3004068 | Inorg. Chem. 2012, 51, 7598−7608

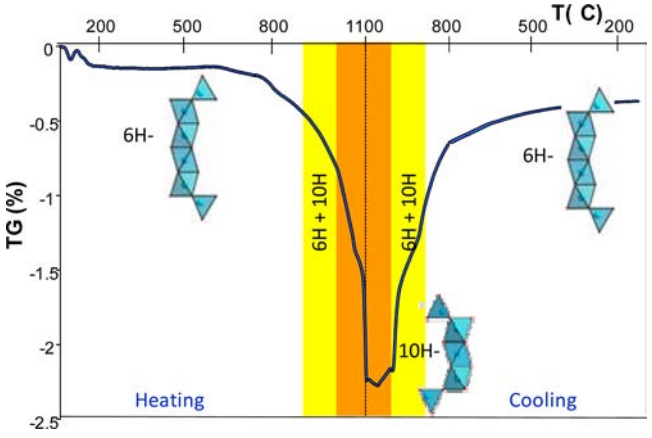


**Figure 3.** Thermogravimetric analysis of 6H–$Ba_6Co_6Cl_{1-x}O_{16-\delta}$ showing a phase transformation above 1000 °C into 10H–$Ba_5Co_5Cl_{1-x}O_{13-\delta}$.

redox titrations (oxochloride: 6H; $Co^{+3.37}$ → 10H; $Co^{+3.24}$, oxofluoride: 6H; $Co^{+3.36}$ → 10H; $Co^{+3.20}$).

*Co/Fe Oxohalides.* The $Ba_5Co_{5-y}Fe_yXO_{1-\delta}$ samples have been prepared in two different ways: slow cooling or quenching from 900 °C (F case) or 1000 °C (Cl case) as detailed in the Experimental Procedures section. The identification of XRD patterns evidence that, independently of the thermal route, the 10H-polymorph (trimeric, $n = 3$) is exclusively formed even for a low Fe-doping ratio. The optimizations of the XRD profile and lattice parameters were carried out in the space group of the 10H Co parent compound ($P6_3/mmc$).

**3.b. Cationic Distribution.** The enlargement of the unit cell parameters follows the introduction of larger Fe-cations (Figure 4a, Table 1). Powder neutron diffraction was used to accurately refine the Fe/Co distribution, taking advantage of the strong Fermi-length contrast. The results of the refinements are listed in Table 2. We note for the compound $Ba_5Fe_4Co_1ClO_{\sim 13}$, the presence of a minor impurity assigned to $Ba_3Fe_2Cl_2O_5$ appears during the preparation of a large amount of powder under air and was revealed after ND while this impurity was barely detected by XRD. After a preliminary pattern matching stage, the original atomic structure is introduced. After adjustment of the atomic positions, the mixed Fe/Co cationic site occupations were refined with respect to the full occupancies of all metal sites. After refinement of the isotropic thermal parameters, the occupancies of the anions were refined. For the $y = 2$ and $y = 3$ terms (F) and $y = 4$ (Cl), a magnetic contribution was also considered at room temperature. A lowest Fe ratio was refined in the central M2 octahedral site comparatively to the surrounding M1 octahedra and M3 tetrahedra. A similar behavior for Fe was already observed in the mixed metallic oxide 6H′–$BaMn_{0.85}Fe_{0.15}O_{2.87}$.[20] In the $y = 0$ Co compounds, a HS $Co^{3+}$ in tetrahedral coordination and LS $Co^{3+/4+}$ in octahedral coordination was proposed from DFT-band structure analysis.[21] In the $Ba_5Fe_yCo_{5-y}X_{1-x}O_{13-\delta}$ system, we still attribute the tetrahedral Co3 to HS-$Co^{3+}$, but the valence state of the concomitant Fe3 is rather uncertain, taking into account the great stability of both $Fe^{3+}$ and $Fe^{4+}$ in various coordinations.

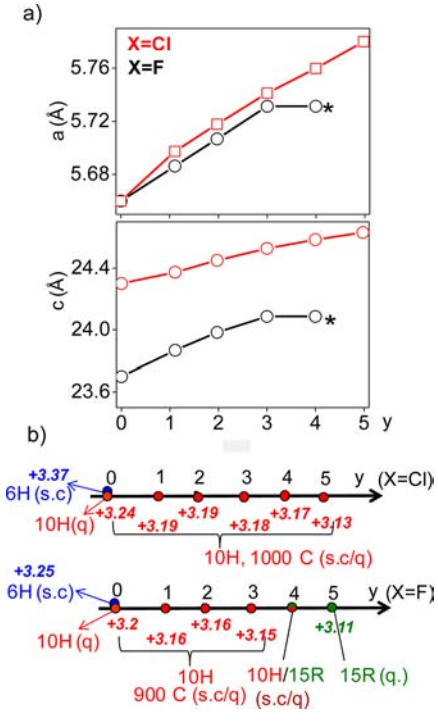


**Figure 4.** (a) Lattice parameters evolution with $y$ for $Ba_5Co_{5-y}Fe_yX_{1-x}O_{13-\delta}$; X = Cl in red; X = F in black. (b) Iodometric titration versus $y$. The synthesis method is denoted by q. (quenched), and s.c. (slowly cooled). ∗ show polyphased samples.

**3.c. Redox Properties.** The titration of the mean "as-prepared" Co/Fe oxidation state performed at short time after synthesis indicates a continuous reduction with increasing $y$ (in relatively good agreement with ND refinements; Figure 4b and Table 1). We note higher oxidation states for oxochloride compounds (from +3.24(1) to +3.17(1)) compared to oxofluorides (from +3.20(1) to +3.11(1)) taking into account the precision on the titration. For both series, even taking into account a possible halogen-site deficiency, it involves a significant concentration of oxygen vacancies. In detail, in the four terms studied by PND, the following observations can be given regarding the oxygen occupancy (Table 2):

- O1 sites of the cubic layers are partially filled (occ. from 94% to 99%).
- O2 sites of the hexagonal layers are completely filled.
- O3 atoms of the $h'$-layers, which form the axial corners of the tetrahedra, are slightly off-centered from their ideal special position as already shown for the parent $Ba_5Co_5F_{1-x}O_{13-\delta}$. Significant amounts of vacancies were refined for this splitted site (refined occ. from 87% to 96%). This particular point should be considered carefully, taking into account the residual nucleon density in h′-layers discussed later; it suggests a certain degree of in-plane disorder.
- Finally, we note that, as already observed on $Ba_5Co_5FO_{13-\delta}$,[21,4] off-centered F atoms are observed, i.e., the fluorine atom was displaced from its central 2$c$ (1/3, 2/3, 1/4) to a 6$h$ 2$x$, $x$, 1/4) position, ∼1/3 occupied (Table 2), validated by an improvement of the agreement factors. This assumption was first tested for $Ba_5FeCo_4FO_{13-\delta}$ (paramagnetic at room temperature) and then applied to all the other terms. Contrarily, in the oxo-chlorine case (PND data available for $Ba_5Fe_4Co_1ClO_{13-\delta}$), a similar peripheral split of Cl increases the agreement factors, so they were kept in their central position.

**3.d. Vacancies and *h*′-Disorder.** The deficient character of the cubic $c$-layers preferentially to the hexagonal-layers is consistent with what is observed in the $BaCoO_{3-\delta}$ polytypes and contradict the main behavior of $BaMnO_{3-\delta}$ polytypes. Once more, we recall


dx.doi.org/10.1021/ic3004068 | Inorg. Chem. 2012, 51, 7598–7608

**Table 2. Neutron Diffraction Rietveld Refinement**[a]

| Atom | Wyck. | Occ. | *x* | *y* | *z* | $U_{iso}$ (Å$^2$) compound |
|---|---|---|---|---|---|---|
| Ba1 | 2b | 1 | 0 | 0 | 1/4 | 0.0096(6) (1) |
| | | | | | | 0.0071(5) (2) |
| | | | | | | 0.0291(2) (3) |
| | | | | | | 0.0142(4) (4) |
| Ba2 | 4f | 1 | 1/3 | 2/3 | 0.1361(2) | 0.0085(6) |
| | | | | | 0.1360(2) | 0.0065(4) |
| | | | | | 0.1352(1) | 0.0046(5) |
| | | | | | 0.1273(2) | 0.0154(3) |
| Ba3 | 4f | 1 | 2/3 | 1/3 | 0.0389(2) | 0.0096(5) |
| | | | | | 0.0377(2) | 0.0071(5) |
| | | | | | 0.0381(1) | 0.0080(7) |
| | | | | | 0.0380(2) | 0.0139(4) |
| Co1/Fe1 marginal octahedra | 4e | 0.637(5)/0.213(5) | 0 | 0 | 0.1029(2) | 0.0050(1) |
| | | 0.560(1)/0.440(1) | | | 0.1041(1) | 0.0108(9) |
| | | 0.426(5)/0.674(5) | | | 0.1060(1) | 0.0076(5) |
| | | 0.826(8)/0.174(8) | | | 0.1071(8) | 0.0051(2) |
| Co2/Fe2 central octahedra | 2a | 0.972(8)/0.028(8) | 0 | 0 | 0 | 0.0050(2) |
| | | 0.840(9)/0.160(9) | | | | 0.0027(2) |
| | | 0.701(9)/0.299(9) | | | | 0.0075(1) |
| | | 0.617(8)/0.383(8) | | | | 0.0049(2) |
| Co3/Fe3 tetrahedra | 4f | 0.768(5)/0.232(5) | 2/3 | 1/3 | 0.1782(2) | 0.0107(1) |
| | | 0.530(1)/0.470(1) | | | 0.1780(1) | 0.0072(7) |
| | | 0.260(6)/0.740(6) | | | 0.1779(2) | 0.0116(4) |
| | | 0.167(7)/0.833(7) | | | 0.1758(9) | 0.0047(2) |
| O1 | 12k | 0.938(8) | 0.8391(2) | 0.6782(4) | 0.1501(1) | 0.0112(2) |
| | | 0.970(6) | 0.8390(3) | 0.6780(6) | 0.1501(1) | 0.0113(3) |
| | | 0.946(4) | 0.8391(1) | 0.6782(2) | 0.1501(1) | 0.0103(9) |
| | | 0.984(5) | 0.8351(2) | 0.6712(4) | 0.1479(8) | 0.0113(2) |
| O2 | 12k | 0.987(8) | 0.1471(2) | −0.1471(2) | 0.0501(1) | 0.0112(2) |
| | | 1 | 0.1493(2) | −0.1493(2) | 0.0501(1) | 0.0113(3) |
| | | 1 | 0.1490(2) | −0.1490(2) | 0.0498(9) | 0.0103(9) |
| | | 1 | 0.1491(3) | −0.1491(3) | 0.0475(9) | 0.0113(2) |
| O3 | 6 h | 0.319(5) | 0.7364(2) | 0.3682(1) | 1/4 | 0.0112(2) |
| | | 0.310(6) | 0.7312(4) | 0.3651(2) | | 0.0113(3) |
| | | 0.293(5) | 0.7520(6) | 0.3760(3) | | 0.0103(9) |
| | | 0.300(5) | 0.7298(4) | 0.3649(2) | | 0.0113(2) |
| F | 6 h | 0.330(5) | 0.3009(6) | 0.6018(3) | 1/4 | 0.0469(4) |
| | | 0.333(3) | 0.2941(4) | 0.5882(2) | | 0.0407(4) |
| | | 0.317(5) | 0.2930(4) | 0.5860(2) | | 0.0487(1) |
| Cl | 2c | 0.848(8) | 1/3 | 2/3 | 1/4 | 0.0262(1) |

[a]Each item is given for four compounds as follows: (1) $Ba_5Co_4Fe_1F_{1-x}O_{13-\delta}$ → refined formula: $Ba_5(Co_{4.02}Fe_{0.98})F_{0.98}O_{12.51}$ $R_{Bragg}$ = 6.27%, $R_F$ = 4.70%. (2) $Ba_5Co_3Fe_2F_{1-x}O_{13-\delta}$ → refined formula: $Ba_5(Co_{3.02}Fe_{1.98})F_1O_{12.75}$, $R_{Bragg}$ = 5.83%, $R_F$ = 3.94%, $R_{mag}$ = 16.2%. (3) $Ba_5Co_2Fe_3F_{1-x}O_{13-\delta}$ → refined formula: $Ba_5(Co_{2.01}Fe_{2.99})F_{0.95}O_{12.55}$ $R_{Bragg}$ = 5.83%, $R_F$ = 3.94%, $R_{mag}$ = 16.2%. (4) $Ba_5Co_1Fe_4Cl_{1-x}O_{13-\delta}$ → refined formula: $Ba_5(Co_{3.9}Fe_{1.1})Cl_{0.85}O_{12.80}$ $R_{Bragg}$ = 3.46%, $R_F$ = 2.25%, $R_{mag}$ = 7.51%; * = impurity $Ba_3Fe_2Cl_2O_5$.

that in this system the vacancies prefer the *h*−[$BaO_{3-\delta}$] layers, the low concentration of hexagonal sequence in the most reduced crystal structures.[9] It creates strongly deficient *h*-layers in the most reduced terms, e.g., *h*−[$BaO_{2.25}$] in the 4H−$BaMnO_{2.65}$ with stacking sequence $(hc)_2$.[11] In the title series, the presence of oxygen vacancies in the *c*−[$BaO_{3-\delta}$] and in the *h*′−[$BaX_xO_{1-\delta}$] layers questions the $CoO_{4-z}$ coordinations, which locally lose their tetrahedral configuration. The mechanism that we propose is based on the observation of Fourier difference maps in the *h*′-layers. For instance, at room temperature, the difference-Fourier maps for $Ba_5Fe_1Co_4FO_{13-\delta}$ reveals high residual nucleon densities on three positions at ≈1.17 Å from the ideal F-position and at ≈1.26 Å from the ideal O-position. Then, a "*push−and−pull*" mechanism (Figure 5) can be proposed implying that the creation of vacancies in upper O1 sites leads to the partial displacement of F atoms within the M3 sphere of coordination, while the neighboring O atoms are pushed forward. In such a case, we could reasonably estimate basal F−O distances to about 2.62 Å (from residual Fourier peaks) instead of the ideal 3.27 Å. Then a part of the $(Co/Fe)O_4$ tetrahedra transform into distorted $(Co/Fe)\square_1O_3F$ polyhedra (□ = oxygen vacancies). At the same time, in-plane Ba atoms are displaced to relax interatomic constraints, as shown by residual nucleon densities around the Ba-sites. This effect is favored in the oxofluoride case, accordingly to the easy delocalization of $F^-$ compared to that of $Cl^-$ in the basal *h*′-layer.

## 4. THERMAL BEHAVIOR

The recent investigation of hexagonal 6H/15R and tetragonal $(Ba,Sr)FeF_yO_{3-\delta}$ polytypes has evidenced atypical oxygen exchange at temperatures as low as 200 °C.[12,22] To probe


dx.doi.org/10.1021/ic3004068 | Inorg. Chem. 2012, 51, 7598−7608

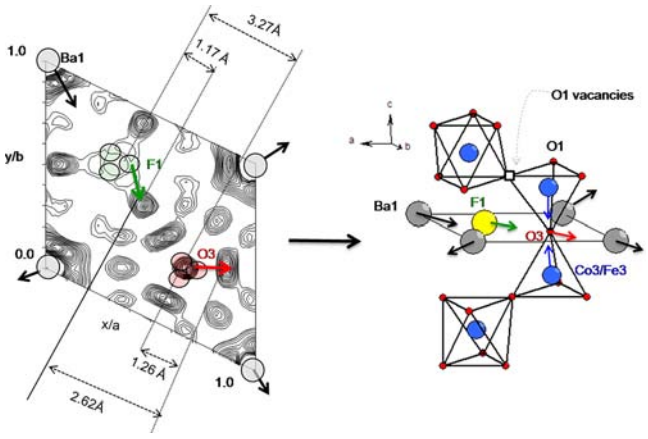


**Figure 5.** Fourier difference map of the *h*′-layer after PND Rietveld refinement of $Ba_5Co_1Fe_4F_{1-x}O_{13-\delta}$ (left); the residual nucleon density is pictured by the "*push-and-pull*" mechanism (right).

similar singularities in the 10H-oxohalide systems, thermogravimetric analyses (TGA) have been completed on several samples (Supporting Information, Table S1) using two consecutive heating/cooling cycles (cycle 1 and 2 in Figure 6). Measurements

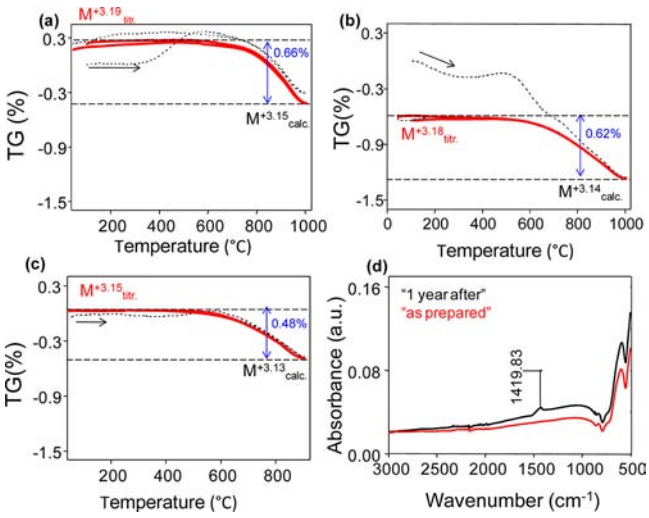


**Figure 6.** Thermogravimetric analysis of (a) $Ba_5Co_4Fe_1Cl_{1-x}O_{13-\delta}$, (b) $Ba_5Co_2Fe_3Cl_{1-x}O_{13-\delta}$, and (c) $Ba_5Co_2Fe_3F_{1-x}O_{13-\delta}$ with valence at RT from redox titration and at HT from TG curves. The first cycle is shown in dotted lines. Reproducibility is achieved at the second cycle shown in red; (d) IR analysis for $Ba_5Co_2Fe_3ClO_{13-\delta}$ just after synthesis (red) and one year after (black) with evidence of carbonates at 1419.83 $cm^{-1}$ (= $\nu_{AS}$).

have been performed up to 1000 °C for oxo-chlorides and up to 900 °C for oxo-fluorides with respect to the thermal stability of each series detailed in the Supporting Information (Figures S2, S3, S4). Typical TGA-plots (after air-exposure during variable time) are presented for the compounds $Ba_5Fe_1Co_4ClO_{13-\delta}$, $Ba_5Fe_3Co_2ClO_{13-\delta}$, and $Ba_5Fe_3Co_2FO_{13-\delta}$. We also give the metal valence corresponding to redox titrations and those at high temperature deduced from the experimental weight-loss, assuming solely oxygen exchange with air. One can generalize the mean behavior step-by-step as follows:

**4.a. First Heating Ramp.** This seems to adopt variable behavior, independently on the Fe/Co ratio, or on the X (= F or Cl) nature. It sometimes shows a primary oxidation wave (Figure 6a), while some samples display a normal weight loss (up to 0.3% until 600 °C) (Figure 6b) or a weight conservation (Figure 6c). This behavior most probably reflects water/carbonate sorption in air. Infrared spectra measured for "as-prepared" and "long-time air-exposed" samples clearly show the evidence of carbonate groups in the latter (Figure 6d). Furthermore, in most cases, a primary inflection point around 500−600 °C is observed. Then multiple phenomena could interact. The disparities (exaggerated for the Cl compound) validate a time-dependent evolution. In fact, titrations performed at different lifetime of the samples show sensitive evolutions that will not be discussed in the scope of our paper. At least we check that titration after a high-temperature treatment (TGA, for instance) gives results in good agreement with the "as-prepared" state. For these reasons, we will focus on the next thermal cycles (end of heating 1 + cooling + heating/cooling 2) that seem common to all compounds; indeed, all the samples show an important reduction/reoxidation on heating above 600 °C and subsequent thermal ramps.

**4.b. Next Cooling/Heating Ramps and Thermal Structural Changes.** The mean reduction/reoxidation is fully reversible for all the samples and highlights an invariant-redox plateau between 500 °C and room temperature. Generally, the amplitude of the TGA weight loss between the RT and the HT states corresponds to a sensitive reduction from $M^{n+}$ to $M^{(n-0.15)+}$. High temperature XRD analyses have been performed on several samples to correlate the results of TGA investigations (first irreversible cycle, reduction/reoxidation evidence) with the changes of the lattice parameters. For this, results of the thermodiffraction experiments from RT until 1000 °C for oxo-chloride compounds/until 900 °C for oxo-fluoride and back to RT are informative. Typical results are shown on the Figure 7a and b for one oxo-chloride and one oxo-fluoride, respectively. In contrast to what was observed from the first ramp of the TGA, the evolution of the hexagonal *a* and *c* parameters is monotone and reflect a predominant standard thermal expansion effect that could be combined with a minor lattice dilatation due to reduction (on heating), increase of the mean M ionic radius, and contraction during reoxidation (on cooling). However, slight anomalies are observed around 600 °C, the temperature at which the TGA first cycle shows the discussed concavity, but their amplitudes are weak in regard to the full evolution parameters. On the other side, the *in situ* Rietveld analysis is more conclusive, and we paid particular attention to the evolution of the M−M distances (M = Fe/Co in the various offered crystal positions).

This reveals a diminution of the d3 (M3−M3) separation inside the tetrahedral dimers (at both sides of the *h*′-layers) on heating for both the Cl and F compounds (Figure 8a,b), with this expansion being particularly reinforced in the F case. It also appears that the other M—M separations projected on the *c*-axis almost shows the expected dilatation on heating and contraction on cooling. One must conclude that reduction on heating mainly concerns tetrahedral oxygen atoms. Accordingly to the "*push-and-pull*" mechanism proposed in Figure 5 from RT data, the lowering of the d3 separation then results essentially from the exaggerated creation of vacancies in *c*- and *h*′-layers and subsequent local distortion of the $(Fe/Co)_2O_7$ pairs of tetrahedral. Besides, opening M3−O3−M3 angle out of the ideal 180° drives the M3−M3 shortening.

Also the heating/cooling miss-reversibility validates slight redox changes between the *initial* and *cooled-back* states, despite unmodified lattice parameters. This point results probably from the evolution at room temperature of the samples discussed in


dx.doi.org/10.1021/ic3004068 | *Inorg. Chem.* 2012, 51, 7598−7608

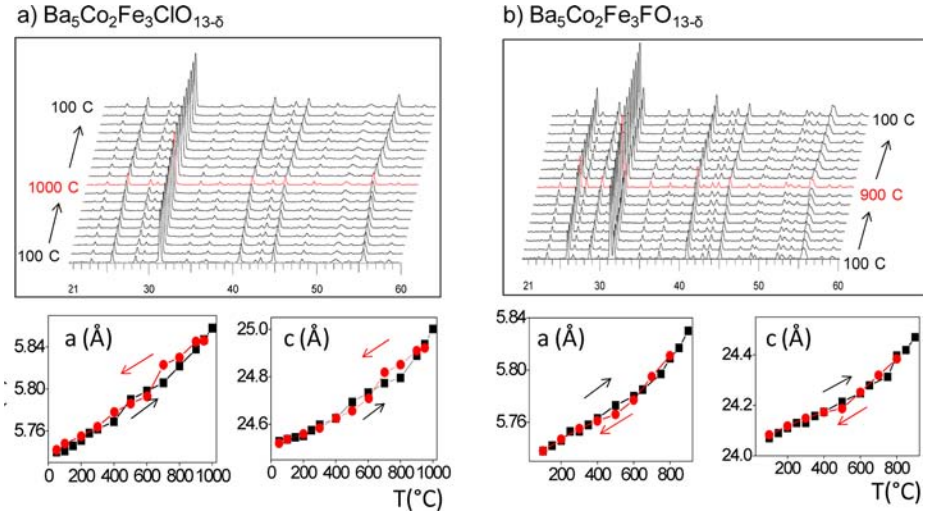


**Figure 7.** Thermodiffractograms and cell parameters evolution upon heating (black) and cooling (red) for (a) $Ba_5Co_2Fe_3ClO_{13-\delta}$ and (b) $Ba_5Co_2Fe_3FO_{13-\delta}$.

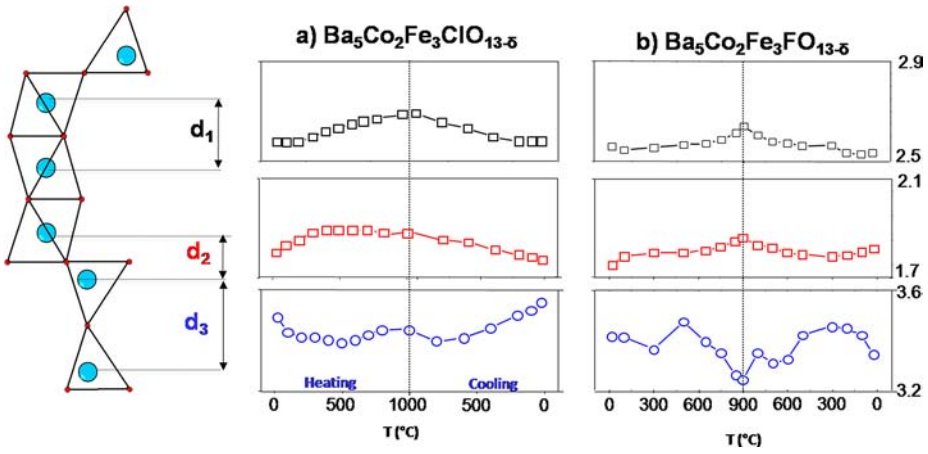


**Figure 8.** Intermetallic separation projected along the *c*-axis upon heating and cooling for (a) $Ba_5Co_2Fe_3ClO_{13-\delta}$ and (b) $Ba_5Co_2Fe_3FO_{13-\delta}$.

Section 4a taking into account that the HT-XRD- checked samples were not "freshly"-prepared phases.

## 5. TRANSPORT PROPERTIES OF $Ba_5(Co,Fe)_5XO_{13-\delta}$ (X = F, Cl)

The electric resistivities at low temperature are given in Figure 9a and b. All the terms of the oxo-chlorides and oxo-fluorides solid solutions show an insulating character. As a general statement, the resistivity increases with the Fe content. The substitution of Co for Fe is expected to localize electrons into more insulating systems. Also, it should be remembered that the lattice dilatation that accompanied the Fe incorporation plays in favor of limited interatomic overlapping and electrons hopping. In fact, similar transport evolution was already reported for $La_{0.6}Sr_{0.4}Co_{1-y}Fe_yO_3$ ($y$ = 0 to 1.0) solid solution.[23] Because transport measurements on Fe/Co compounds have been measured on polycrystalline samples, one should be very careful about their interpretation. However, by comparison between the Arrhenius behavior (linear $\log(\rho)$ vs $T^{-1}$ law) and 1D-variable range hopping (VRH) mechanism (linear $\log(\rho)$ vs $T^{-1/2}$), the rough linearity of the second suggests a transport possibly governed by localized electronic states (Figure 9).[24] Particularly, the $T^{-1/2}$ dependence suggests a mono- dimensional conductivity type "Hopping 1D" probably along the *c*-axis favored by the structural anisotropy in these materials and linear strings growing along *c*. The same behavior was observed in the case of the related 6H–$Ba_6Co_6ClO_{16-\delta}$ compound.[25] For the 10H–$Ba_5Co_5ClO_{13-\delta}$ compound, a greater conductivity along *c* was measured on a single crystal[26] in good agreement with a mono-dimensional transport.

## 6. MAGNETISM

**6.a. Magnetic Susceptibility.** All the prepared compounds (Figures S5 and S6, Supporting Information) are antiferromagnetic below $T_N$, this latter being strongly dependent on the $y$ Fe content. The approximated Néel temperatures and Curie–Weiss parameters are listed in Table 3 but should be considered with precaution. Indeed, it is noteworthy that for all Co parent oxohalides there was already evocated the unclear distinction of $T_N$[7] from thermal susceptibility plots. At this level, the substitution of Co for Fe does not clarify the situation. For instance, Figure 10a shows $\chi_m(T)$ and $\chi^{-1}{}_m(T)$ for $y$ = 1, X = F, in which the weak anomaly at $T \sim 280$K is assigned to the magnetic-ordering temperature in good agreement with low-temperature ND data ($T_N$ = 250 K) to be further presented. In more ambiguous cases, several anomalies can be observed such that the $T_N$ was chosen following a regular increase of $T_N$ with increasing $y$, e.g,. $y$ = 3, X = F (Figure 10b). In general,


dx.doi.org/10.1021/ic3004068 | Inorg. Chem. 2012, 51, 7598–7608

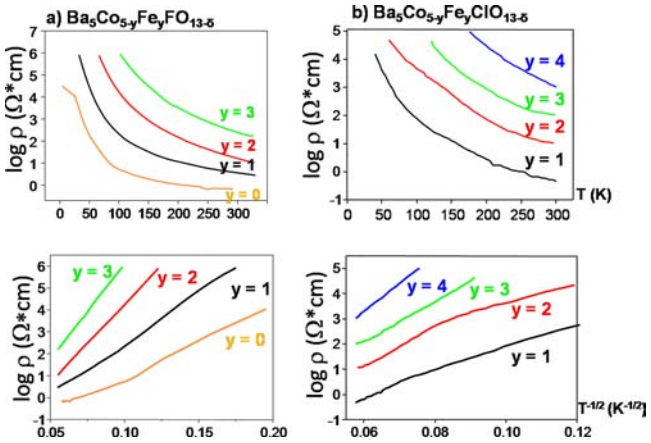


**Figure 9.** Resistivity logarithm evolution with $T$ and $T^{-1/2}$ for (a) $Ba_5Co_{5-y}Fe_yFO_{13-\delta}$ and (b) $Ba_5Co_{5-y}Fe_yClO_{13-\delta}$.

the poor $T_N$ distinction results from HT VSM data. Particularly, increasing the Fe content increases $T_N$ such that the investigated paramagnetic domain is restricted for an unambiguous linear regression of the Curie–Weiss parameters. Also, the thermal behavior discussed above (oxygen exchange with air) is expected to alter our high-temperature measurements performed under flowing air. Clearly, the evolution of the effective moment with the Fe content does not respect the expected behavior (theoretical $\mu_{eff}$ are listed in Table 3 for $Co^{3+}{}_{HS}$ (S = 2) in tetrahedra, $Co^{3+}{}_{LS}$ (S = 0) in octahedra, and $Fe^{3+}{}_{HS}$ (S = 5/2) in both environments accordingly to the Fe/Co distribution). Graphically, in Figure 10b and c, for $y$ = 3, X = F, and for $y$ = 3, X = Cl, respectively, highlights the poor precision on the listed $\mu_{eff}$ values; the relatively large negative Curie–Weiss temperatures validate predominant antiferromagnetic exchanges.

Finally, one should mention that even if in most cases the magnetizations M(H) below $T_N$ present no residual magnetic moments (Figure 10d,f), some compounds such as $y$ = 2, X = F, and $y$ = 3, X = F, display a weak ferromagnetic component (typically a remanent moment of 0.01 $\mu_B$ at $T$ = 296 K for $y$ = 3, X = F (Figure 10e). It could result for several disorder aspects related to the Fe/Co distribution and to the competition between FM and AFM exchanges while Co–Co, Fe–Fe or Co–Fe interact. Also, the presence of a small amount of FM impurities cannot be excluded, especially dealing with Fe-based oxo-halides.

The most striking point about $Ba_5Co_{5-y}Fe_yXO_{13-\delta}$ solutions concerns the high $T_N$ observed after introduction of a significant amount of Fe (for $y$ = 3, X = Cl, $T_N$ around 560 K). Recently, it has been established for fluorinated 6H and 15R Fe-perovskites by DFT calculations[27] that this behavior is mainly driven by strong magnetic exchanges at the Fe–O–Fe tetrahedral junction. At this level, the mean interatomic topology (Fe–O–Fe ~180°) is consistent with Kanamori–Goodenough (KG) rules[28] that predict strong AFM superexchanges for $Fe^{3+}$ cations.

**6.b. Effect of Fe Introduction on the Magnetic Structure.** Low-temperature PND data have been collected for $y$ = 1, 2, 3 (X = F) and for $y$ = 4 of (X = Cl). The 3D-magnetic ordering is demonstrated by the increase in the intensity of peaks below $T_N$. They overlap nuclear-Bragg angles, such that the nuclear periodicity is conserved by the magnetic structure. (propagation vector: $k$ = 0,0,0). Because of the dipolar nature of the spin-neutron interaction, the diffracted magnetic intensity concerns the component of the spins perpendicular to the scattering vector. Then the absence of 00$L$ magnetic components suggests the orientation of the spins along the $c$-axis.

By analogy with the parent compounds (FM intrablock, AFM interblock), we first tried to refine similar models for the Fe-doped terms. These models did not converge, and adding an extra degree of freedom for the spins give raise in each case to a AFM site-to-site interaction, as shown in Figure 11a and b. The thermal evolutions of magnetic moments are represented in the Figure 11c. The values at 1.5 K are listed in Table 3 with the corresponding reliability factors for the four investigated compounds. This result is all the more astonishing that it concerns each of the refined compounds, even with low Fe content ($y$ = 1).

In few points, the principal characteristics of the established magnetic structures are as follows:

1 As in the case of parent Co-compounds, the tetrahedral atoms display the larger magnetic moments.
2 An increase of the magnetic moments with the Fe ratio is observed on the M1 and M2 octahedral sites. It particularly concerns the marginal M1 site, which shows for the parent–$Ba_5Co_5XO_{13-\delta}$, null (X = F) or very low (X = Cl, $M_{Co1}$ = 0.6 $\mu_B$) magnetic moments.[7] It

**Table 3. Magnetic Data for $Ba_5Fe_yCo_{5-y}XO_{13-\delta}$ from M/H($T$) Plots and Low-Temperature Neutron Diffraction**[a]

| | | | magnetic susceptibility | | | neutron diffraction M ($\mu_B$) at 1.5 K | | |
|---|---|---|---|---|---|---|---|---|
| | $y$ | $T_N$ (K) | $\mu_{eff}$ ($\mu_B$/f.u.) | $\mu_{eff\ th}$ ($\mu_B$/f.u.) | $\theta_{CW}$ (K) | Co1/Fe1 | Co2/Fe2 | Co3/Fe3 |
| **F** | 0 | 122 | 6.97* | 10.95 | −311* | 0.57(9) | 0.44(8) | 2.47(5) |
| | 1 | ≈280 | ≈8.0 | 11.44 | ≈−500 | 0.73(9) | 0.46(8) | 2.68(5) |
| | 2 | ≈470 | ≈7.5 | 11.91 | ≈−300 | 1.29(5) | 0.92(6) | 3.02(4) |
| | 3 | ≈520 | ≈7.5 | 12.36 | ≈−300 | 2.50(6) | 1.39(5) | 3.37(7) |
| **Cl** | 0 | 126 | 9.21* | 10.95 | −766* | 0.61(7) | 0.35(8) | 2.21(8) |
| | 1 | ≈200 | ≈6.5 | 11.44 | ≈−250 | | | |
| | 2 | ≈440 | ≈8.5 | 11.91 | ≈−600 | | | |
| | 3 | ≈560 | ≈7.5 | 12.36 | ≈−250 | | | |
| | 4 | ≈520 | not linear | 13.23 | not linear | 3.42(6) | 1.64(7) | 4.07(7) |
| | 5 | $Fe_3O_4$ impurity | | | | | | |

[a] $T_N$ and Curie–Weiss parameters are roughly estimated except when marked by ∗ (data from ref 7).


dx.doi.org/10.1021/ic3004068 | Inorg. Chem. 2012, 51, 7598–7608

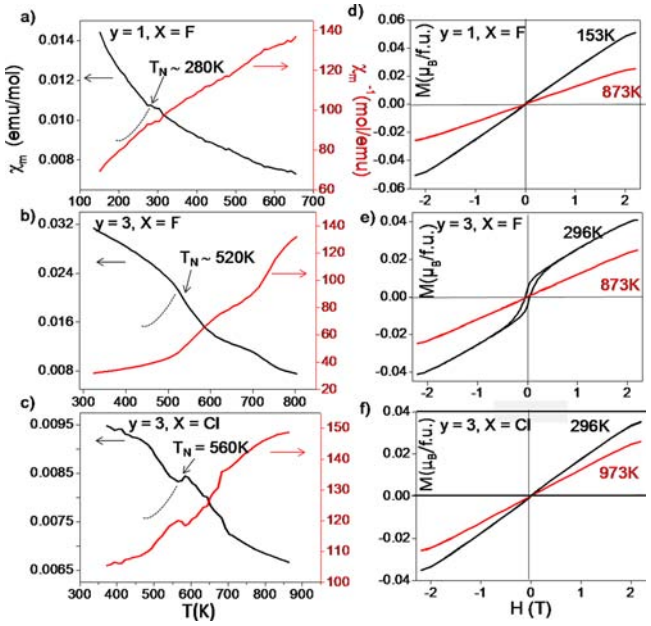


**Figure 10.** Magnetic susceptibility $\chi_m$ (emu/mol) and $\chi_m^{-1}$ (mol/emu) at 0.2T for (a) $Ba_5Co_4FeFO_{13-\delta}$, (b) $Ba_5Co_2Fe_3FO_{13-\delta}$, and (c) $Ba_5Co_2Fe_3ClO_{13-\delta}$. The $T_N$-dotted lines are guides for the eye. (d–f) Corresponding magnetization plots at both sides of the AFM transition.

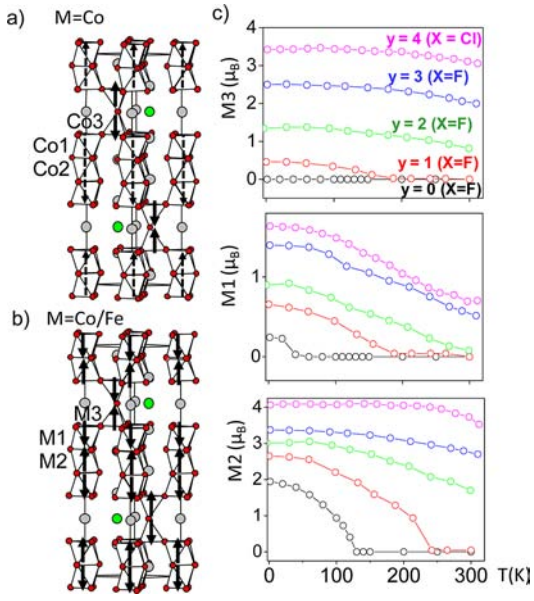


**Figure 11.** Magnetic structure of (a) $Ba_5Co_5XO_{13\_\delta}$, (b) mixed $Ba_5Co_{5-y}Fe_yXO_{13-\delta}$ compounds, and (c) magnetic moments evolution for mixed sites M1, M2, M3.

follows the weak occupancy of M1 by Fe, while M2 hosts a significant amount of Fe.

3 Similar to previous deconvolution of the magnetic structure in elementary exchanges reported for the 6H–$Ba_6Co_6ClO_{13-\delta}$ on the basis of simple exchange rules,[25] we can rationalize the mixed 10H–Fe/Co magnetic ordering as follows:

4- between two blocks, corner-sharing tetrahedral Co–O–Co is observed strongly AFM. At the origin of the high $T_N$ discussed above, the local introduction of Fe reinforces this feature, predictable from KG rules at least for $Fe^{3+}$ species.

5- in the block, the tetrahedral/octahedral connection is FM that was predicted from KG rules for a Co–O–Co angle close to 180°. Apparently, the incorporation of Fe, even in a small ratio ($y = 1$) is sufficient to turn these exchanges into AFM exchanges at this level.

6- finally, the FM coupling observed between weak moments inside the Co face-sharing strings was previously assigned to important electronic delocalization due to metal–metal bondings (→ FM direct exchanges) and low-spin configuration of $Co^{3+}$ and $Co^{4+}$ in the strings. Here, the introduction of Fe is supposed to break such exchanges by strong electronic localization due to the different Co and Fe nature (see the Transport Properties section). In such case the 180 °Co–O–Fe superexchange should predominate, and the observed negative couplings is similar to what was previously observed at the tetrahedral/octahedral connection.

## 7. DFT

About this last point, a more circumspect analysis of the linear strings of the Co-parent compounds can be performed in regard to first-principles calculation on the 1D-$BaCoO_3$.[29] Here, the hypothetical direct exchange effects along face-sharing octahedral chains are refuted, while the magnetic electron of LS $Co^{4+}$ are ordered on alternatively $dx^2 - y^2$ and $dxy$ orbitals along the 1D-chain. Then FM $Co^{4+}$–O–$Co^{4+}$ superexchange dominates. To clarify the origin of the low-ordered moment in the octahedral sites in the $Ba_5(Co,Fe)_5XO_{13-\delta}$ systems, DFT calculations were performed for $Ba_5Fe_2Co_3FO_{13}$ comparatively to $Ba_5Co_5FO_{13}$. Clearly, we aim to estimate local magnetic moments and to probe the most probable electronic configuration and oxidation states of the sites along the string direction for both M=Co and Fe. In particular, to evaluate the electronic contribution after the Fe substitution without any structural modifications, an ideally ordered $Ba_5Fe_2Co_3FO_{13}$ model was built with Fe atoms placed in M1 sites while M2 and M3 sites were kept filled with Co. Results are compared to previous results for nondoped $Ba_5Co_5FO_{13}$.[21] As already extensively discussed in the latter, despite the fact that $Ba_5(Fe,Co)_5FO_{13}$ compounds are insulators, GGA as well as GGA+U did not allow the opening of a gap for the Fe-substituted compound. However, for our purpose, the general features of the electronic structure obtained by GGA are sufficient to discuss the most probable oxidation states and spin configurations at the different transition metal sites. Therefore, we focus on the electronic structure obtained in GGA only.

The plots of the calculated Density of States (DOS) projected on the d states for the Fe(1) and Co(2) sites are represented in Figure 12. For comparison, the DOS reported for the same sites for the nonsubstituted compound (Co1 and Co2) are represented in Figure 12c and d.

i) The tetrahedral moment (Co3 site) was intensively discussed for $Ba_5Co_5FO_{13}$ and clearly corresponds to HS $Co^{3+}$.[21]This result remains unchanged after Fe incorporation in neighboring octahedral sites.

ii) For Fe on the M1 site, the up-spin levels are almost all occupied, while the down-spin states are empty such that Fe1 is best described by a high-spin $d^4$ configuration (i.e.,


dx.doi.org/10.1021/ic3004068 | Inorg. Chem. 2012, 51, 7598–7608

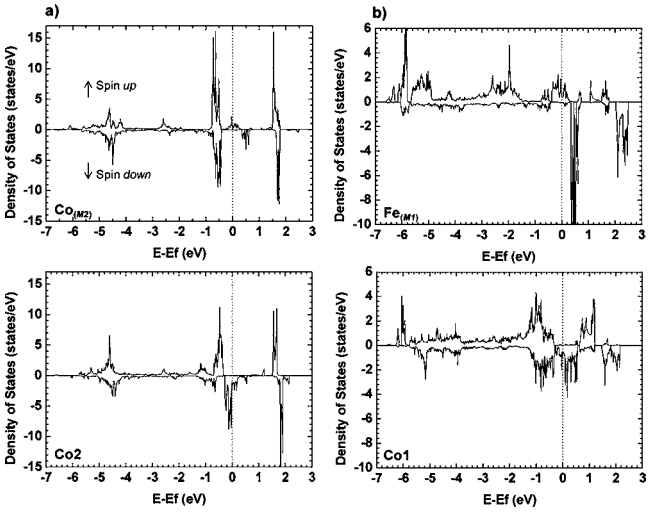


**Figure 12.** Density of States projected on the d orbitals of (a) Co in the M2 site of the substituted structural model $Ba_5Fe_2Co_3O_{13}F$ and Co2 in the nonsubstituted compound $Ba_5Co_5O_{13}F$ and (b) Fe in the M1 site of $Ba_5Fe_2Co_3O_{13}F$ and Co1 in $Ba_5Co_5O_{13}F$. A vertical dotted line indicates the Fermi level.

HS $Fe^{4+}$). Contrarily, in the undoped compound, Co1 correspond to a LS $Co^{3}/^{4+}$.

iii) For central Co2 sites, the two models present similar DOS-topology. For $Ba_5Fe_2Co_3FO_{13}$, the $e_g$ states are empty, while the $t_{2g}$ states are fully occupied leading to a low-spin $d^6$ picture (i.e., LS $Co^{3+}$). For the nonsubstituted compound, the $e_g$ states are empty and the up-spin $t_{2g}$ states are fully occupied, while the down-spin $t_{2g}$ states are partially empty, such as it is best described in a low-spin $d^5$ configuration.

iv) We also calculated the magnetic moments for the $Ba_5Fe_2Co_3FO_{13}$, e.g., 2.92 $\mu_B$ for Fe1 and 0.11 $\mu_B$ for Co2, which is consistent with the above picture (i.e., HS $Fe(1)^{4+}$ and LS $Co(2)^{3+}$). Note that the relatively low-spin moment 2.92 $\mu_B$ for the Fe site (compared to expected 4 $\mu_B$ for a high-spin $Fe^{4+}$ ion) is probably due to magnetic dilution effect and/or to the calculation method.

Finally, despite favorable short Co−Co ∼2.6 Å separations, our DFT results refute previous assumptions assigning the low local Co moments to partial electronic delocalization confined in the face-sharing trimers.[25] In the case of the nonsubstituted compound, both octahedral Co sites are in localized low-spin states, while experimentally the compound is an insulator. The access to an even more insulating character after Fe incorporation does not computationally modify this scheme for the central Co, while bordering-Fe display HS characteristics. Then, the null/low Co moments along the string direction is clearly of structural origin due to the rhombic local distortion. On the opposite side, Fe conserves a HS configuration in this particular crystal field.

## 8. CONCLUSION

Besides the current interest in the physical properties of cobalt containing oxo-halide perovskites, the Co for Fe substitution provides a significant motivation for understanding the parameters that control the structural edifice. We have shown here that, independently of the synthesis method, mixed (Co,Fe) compounds adopt a 10H−$Ba_5(Co,Fe)_5X_{\sim 1}O_{13-\delta}$ form containing $(Co,Fe)_3O_{12}$ trimeric face-sharing linear chains. This preference against the competing 6H−$Ba_6M_6X_{\sim 1}O_{16-\delta}$ with tetrameric units is explained on the basis of a general argument that assigns shortest linear units for most reduced compounds. Indeed a significant reduction of the mean transition metal valence was observed after Fe incorporation in the parent Co oxo-halides. This result pictures rather well the well-known versatility of $Co^{3+}{}_{1-x}/Co^{4+}{}_x$ systems clearly displaced toward $Fe^{3+}$ in mixed valent $Fe^{3+}{}_{1-x}/Fe^{4+}{}_x$ systems in standard equilibrium conditions. This result gives reliable clues for the prediction within future mixed metal systems. For instance, mixed Co/Mn and Fe/Mn compounds should reasonably lead to dominant 6H forms taking into consideration the great air stability of $Mn^{4+}$ in the perovskites series. Contrarily to previous observations of hexagonal anionic deficient layers $h-[BaO_{3-\delta}]$ in $BaMnO_3$, the agglomeration of vacancies in cubic layers[11] in the investigated systems creates (Co/Fe) tetrahedral deficient polyhedra, likely completed by extra halides anions, at least in the oxo-fluoride systems, i.e., $(Co/Fe)O_3F$ subunits. Also, it supports the tendency to go toward more cubic-rich stacking sequences (trimeric short chains rather than tetrameric ones) for more reduced compounds. Finally, we note strong effects on the physical properties after Fe incorporation that emerges from the interplay between HS Fe species and LS Co species in the linear chains: creation of site to site AFM ordering even for low Fe ratio and pronounced insulating character.

## ■ ASSOCIATED CONTENT

### Ⓢ Supporting Information

One table and 5 figures. This material is available free of charge via the Internet at http://pubs.acs.org.

## ■ AUTHOR INFORMATION

### Corresponding Author

*E-mail: olivier.mentre@ensc-lille.fr.

### Notes

The authors declare no competing financial interest.

## ■ ACKNOWLEDGMENTS

The "Fonds Européen de Développement Régional (FEDER)", "CNRS", "Région Nord Pas-de-Calais", and "Ministére de l'Enseignement Supérieur et de la Recherche" are acknowledged for fundings for the X-ray diffractometers. Nicolas Tiercelin of the IEMN, UMR CNRS 8520, is thanked for his help with magnetic measurements. The authors particularly thank the ANR (Agence Nationale de la Recherche) for financial support of the "*projet-blanc*" MAD-BLAST at the origin of this work.

## ■ REFERENCES

(1) Buttner, R. H.; Maslen, E. N. *Acta Crystallogr. B* **1992**, *48*, 764.
(2) Taguchi, H.; Takeda, Y.; Kanamaru, F.; Shimida, M.; Koizume, M. *Acta Crystallogr. B* **1977**, *33*, 1299.
(3) Darriet, J.; Subramanyam, A. M. *Chem. Mater.* **1995**, *5*, 543.
(4) (a) Yamaura, K.; Cava, R. J. *SSC* **2000**, *115*, 301. (b) Tancret, N.; Roussel, P.; Abraham, F. *J. Solid State Chem.* **2004**, *177*, 1023. (c) Ehora, G.; Renard, C.; Daviero-Minaud, S.; Mentré, O. *Chem. Mater.* **2007**, *19* (12), 2924.
(5) Kauffmann, M.; Roussel, P. *Acta Crystallogr. B* **2007**, *63*, 589.

(6) (a) Boulahya, K.; Parras, M.; Gonzalez-Calbet, J. M.; Amador, U.; Martinez, J. L.; Tissen, V.; Fernandez-Diaz, M. T. *Phys. Rev. B* **2005**, *71*, 144402. (b) Jacobson, A.; Hutchison, J. L. *J. Solid State Chem.* **1980**, *35*, 334.
(7) (a) Mentré, O.; Kauffmann, M.; Ehora, G.; Daviero-Minaud, S.; Abraham, F.; Roussel, P. *Solid State Sci.* **2008**, *10*, 471. (b) Toulemonde, O.; Roussel, P.; Isnard, O.; André, G.; Mentré, O. *Chem. Mater.* **2010**, *22*, 3807.
(8) Iorgulescu, M.; Kabbour, H.; Tancret, N.; Mentré, O.; Roussel, P. *Chem. Commun.* **2010**, *46*, 5271.
(9) Adkin, J. J.; Hayward, M. A. *Chem. Mater.* **2007**, *19*, 755.
(10) (a) Gomez, M. I.; Lucotti, G.; Moran, J. A.; Aymonino, P. J.; Pagola, S.; Stephens, P. W.; Carbonio, R. E. *J. Solid State Chem.* **2001**, *160*, 17. (b) Delattre, J. L.; Stacy, A. M.; Siegrist, T. *J. Solid State Chem.* **2004**, *177*, 928. (c) Grenier, J. C.; Wattiaux, A.; Pouchard, M.; Hazgenmuller, P.; Parras, M.; Vallet − Regi, M.; González − Calbert, J. M.; Alario − Franco, M. A. *J. Solid State Chem.* **1989**, *80*, 6.
(11) Adkin, J. J.; Hayward, M. A *J. Solid State Chem.* **2006**, *179*, 70.
(12) Sturza, M.; Daviero-Minaud, S.; Kabbour, H.; Gardoll, O.; Mentré, O. *Chem. Mater.* **2010**, *22*, 6726.
(13) Rodriguez-Carvajal. *J. Physica B.* **1993**, *192*, 55.
(14) Kresse, G.; Furthmüller, J. *Vienna Ab-initio Simulation Package (VASP)*; Institut für Materialphysik: Vienna, 2004; http://cms.mpi.univie.ac.at/vasp.
(15) Kresse, G.; Joubert, D. *Phys. Rev. B* **1999**, *59*, 1758.
(16) Perdew, J. P.; Wang, Y. *Phys. Rev. B* **1992**, *45*, 13244.
(17) Miranda, L.; Ramirez-Castellanos, J.; Varela, A.; González-Calbet, J.; Parras, M.; Hernando, M.; Fernandez-Diaz, M. T.; Garcia Hernandez, M. *Chem. Mater.* **2007**, *19*, 1503.
(18) Miranda, L.; Feteira, A.; Sinclair, D. C.; Hernández, M. G.; Boulahya, K.; Hernando, M.; Varela, A.; González-Calbet, J. M.; Parras, M. *Chem. Mater.* **2008**, *20*, 2818.
(19) Miranda, L.; Ramírez-Castellanos, J.; Hernando, M.; Varela, A.; González-Calbet, J. M.; Parras, M. *Eur. J. Inorg. Chem.* **2007**, 2129.
(20) Miranda, L.; Sinclair, D. C.; Hernando, M.; Varela, A.; Wattiaux, A.; Boulahya, K.; González-Calbet, J. M.; Parras, M. *Chem. Mater.* **2009**, *21*, 5272.
(21) Mentré, O.; Kabbour, H.; Ehora, G.; Daviero-Minaud, S.; Tricot, G.; Whangbo, M. *J. Am. Chem. Soc.* **2010**, *132* (13), 4865.
(22) Sturza, M.; Daviero-Minaud, S.; Huvé, M.; Renaut, N.; Tiercelin, N.; Mentré, O. *J. Inorg. Chem.* **2011**, *50* (24), 12499.
(23) (a) Mizusaki, J.; Sasamoto, T.; Cannon, W. R.; Bowen, H. K. *J. Am. Ceram. Soc.* **1983**, *66*, 247. (b) Mizusaki, J.; Tabuchi, J.; Matasuura, T.; Yamauchi, S.; Fueki, K. *J. Electrochem. Soc.* **1989**, *136*, 2082.
(24) Mott, N. F. *Philos. Mag.* **1969**, *19*, 835.
(25) Kauffmann, M.; Mentré, O.; Legris, A.; Hébert, S.; Pautrat, A.; Roussel, P. *Chem. Mater.* **2008**, *20*, 1741.
(26) Wang, H.; Yang, J.; Zhang, Z.; Dong, C.; Fang, M. *Phys. Lett. A* **2009**, *373*, 4092.
(27) Sturza, M.; Kabbour, H.; Daviero-Minaud, S.; Filimonov, D.; Pokholok, K.; Tiercelin, N.; Porcher, F.; Aldon, L.; Mentré, O. *J. Am. Chem. Soc.* **2011**, *133*, 10901.
(28) Goodenough, J. B., *Magnetism And The Chemical Bond*, Wiley − Interscience 1963, New − York
(29) Pardo, V.; Blaha, P.; Iglesias, M.; Schwartz, K.; Baldomir, D.; Arias, J. E. *Phys. Rev. B* **2004**, *70*, 1444422.